AIAA JOURNAL
Vol. 47, No. 9, September 2009

Compressible Boundary-Layer Predictions at High Reynolds Number Using Hybrid LES/RANS Methods

Jung-Il Choi* and Jack R. Edwards†
North Carolina State University, Raleigh, North Carolina 27695
and
Robert A. Baurle‡
NASA Langley Research Center, Hampton, Virginia 23681

DOI: 10.2514/1.41598

Simulations of compressible boundary-layer flow at three different Reynolds numbers ($Re_\delta = 5.59 \times 10^4$, 1.78×10^5, and 1.58×10^6) are performed using a hybrid large-eddy simulation/Reynolds-averaged Navier–Stokes method. Variations in the recycling/rescaling method, the higher order extension, the choice of primitive variables, the Reynolds-averaged Navier–Stokes to large eddy simulation transition parameters, and the mesh resolution are considered in order to assess the model. The results indicate that the present model can provide good predictions of the mean-flow properties, second-moment statistics, and structural features of the boundary layers considered. Normalized turbulent statistics in the outer layer are found to be independent of Reynolds number, similar to incompressible turbulent boundary layers.

Nomenclature

A, B	=	constants in van Driest transformation
C_f	=	skin friction
C_{kleb}	=	constant in Klebanoff intermittency function
C_M	=	model constant for subgrid viscosity
C_p	=	specific heat at constant pressure, J/kg · K
C_μ	=	turbulence-model constant
d	=	distance to nearest wall, m
k	=	turbulence kinetic energy, $(\text{m/s})^2$
M	=	Mach number
Pr_t	=	turbulent Prandtl number
p	=	pressure, N/m^2
q	=	flow property
R	=	gas constant, J/kg · K
Re	=	Reynolds number
r	=	wall recovery factor
S	=	strain rate, 1/s
T	=	temperature, K
t	=	time, s
u, v, w	=	velocities in x, y, z directions, m/s
u_j	=	velocity component in coordinate direction j, m/s
u_{vd}	=	van Driest–transformed velocity, m/s
u_τ	=	friction velocity, m/s
x, y, z	=	distances in streamwise, wall-normal, spanwise directions, m
x_j	=	coordinate direction j, m
α	=	turbulence-model constant
Γ	=	blending function
Γ_{kleb}	=	Klebanoff intermittency function
γ	=	ratio of specific heats
Δ	=	filter width, m
δ	=	boundary-layer thickness, m
η	=	ratio of turbulence length scales
θ	=	structure angle
κ	=	von Kármán constant
λ_{ci}	=	swirl strength
μ	=	molecular viscosity, $\text{kg/(m} \cdot \text{s)}$
μ_t	=	eddy viscosity, $\text{kg/(m} \cdot \text{s)}$
ν	=	kinematic viscosity, m^2/s
ν_t	=	kinematic eddy viscosity, m^2/s
Π	=	wake parameter
ρ	=	density, kg/m^3
ϕ	=	turbulence-model constant
χ	=	Taylor microscale, m
Ω	=	vorticity magnitude, 1/s
ω	=	turbulence frequency, 1/s

Subscripts

t	=	turbulent
w	=	wall
0	=	reference condition for boundary-layer thickness
∞	=	freestream

Superscripts

$'$	=	fluctuation
$+$	=	wall coordinates based on local kinematic viscosity and friction velocity

Presented as Paper 4175 at the 38th AIAA Fluid Dynamics Conference, Seattle, WA, 23–26 June 2008; received 14 October 2008; revision received 12 May 2009; accepted for publication 21 May 2009.

*Research Assistant Professor, Department of Mechanical and Aerospace Engineering; jungil_choi@ncsu.edu.

†Professor, Department of Mechanical and Aerospace Engineering; jredward@ncsu.edu. Associate Fellow AIAA.

‡Aerospace Engineer, Hypersonic Airbreathing Propulsion Branch; robert.a.baurle@nasa.gov. Associate Fellow AIAA.

I. Introduction

RECENTLY, high-fidelity models, such as direct numerical simulation (DNS), large-eddy simulation (LES), and hybrid large-eddy/Reynolds-averaged Navier–Stokes (RANS) techniques, have been developed to predict turbulent shock/boundary-layer interactions [1–3]. These methods have shown an ability to directly capture the unsteadiness of the interactions and to improve our understanding of the underlying physics of complicated high-speed flows. Predictions of high Reynolds-number flows still remain a challenging issue in DNS or LES due to the large computational requirements necessary to resolve near-wall turbulence. Because of their use of near-wall modeling, hybrid LES/RANS methods [3–6] offer the potential to compute flows at high Reynolds number with

much less expense than LES or DNS. Accurate predictions would appear to require that most of the boundary layer be computed as a large-eddy simulation, but there has been little work done in determining exactly how well the boundary-layer structure is predicted using these techniques, particularly for high Reynolds numbers.

The objective of the present work is to examine the effects of various modeling and algorithmic parameters on the ability of a representative hybrid LES/RANS method [3] to predict mean-flow and second-moment statistics for a selection of well-characterized compressible turbulent boundary layers. The baseline model uses a flow-dependent blending function to shift the closure from a RANS model (Menter's baseline) [7] near solid surfaces to a large-eddy simulation approach farther away. A key to the performance of the method is the precise embedding of the RANS component of the closure within the boundary layer and the use of recycling/rescaling techniques [3,6,8–11] to sustain the development of larger turbulent structures in the outer layer. To assess the effects of different variations in the formulation, we perform parametric studies based on the flat-plate boundary-layer experiment of Luker et al. [12] ($Re_\delta = 1.78 \times 10^5$ and $M_\infty = 2.80$). These studies vary the position of the average RANS-to-LES transition, the mesh resolution, the higher order extension, and the choice of recycling/rescaling strategy. Finally, the model is used to simulate experiments of Elena and Lacharme [13] ($Re_\delta = 5.59 \times 10^4$ and $M_\infty = 2.32$) and Smits and Muck [14] ($Re_\delta = 1.58 \times 10^6$ and $M_\infty = 2.79$) in order to assess the Reynolds-number independence of the formulation. The numerical methods and physical models used in the investigation are presented in Sec. II. The results of the assessment of the hybrid LES/RANS model and the effects of Reynolds number on turbulent boundary-layer development are discussed in Secs. III and IV, respectively, and some conclusions are presented in Sec. V.

II. Numerical Methods

The governing compressible Navier–Stokes equations are discretized in a finite-volume framework [15]. Inviscid fluxes are discretized using a low-diffusion flux-splitting scheme [16], whereas viscous and diffusive fluxes are discretized using second-order central differences. A dual-time stepping implicit method is used to advance the equations in time. At each time step, a Crank-Nicholson discretization of the equations is solved to a prescribed tolerance using a subiteration procedure. The matrix system resulting from the linearization of the equation system is approximately solved using a planar relaxation procedure at each subiteration. To enhance computational efficiency, matrix elements are evaluated and factored every second time step and are held fixed over the duration of the subiterations.

A. Turbulence Closure

The hybrid LES/RANS model used in the present study [3] is based on Menter's k–ω/k–ε model [7] and only involves modifications to the eddy viscosity description:

$$\mu_t = \rho \nu_t = \rho\left(\Gamma \frac{k}{\omega} + (1-\Gamma)\nu_{t,M}\right) \tag{1}$$

As the blending function Γ approaches 1, the closure approaches its RANS description, and as it approaches zero, a subgrid eddy viscosity is obtained. This work uses a mixed-scale model [17] for the subgrid eddy viscosity, defined as

$$\nu_{t,M} = C_M S^{1/2} (q^2)^{1/4} \Delta^{3/2}$$
$$C_M = 0.06 \quad \text{and} \quad S = \left[\frac{\partial \tilde{u}_i}{\partial x_j}\frac{\partial \tilde{u}_j}{\partial x_i} + \frac{\partial \tilde{u}_i}{\partial x_j}\frac{\partial \tilde{u}_i}{\partial x_j} - \frac{2}{3}\left(\frac{\partial \tilde{u}_i}{\partial x_i}\right)^2\right]^{1/2} \tag{2}$$

An estimate of the subgrid kinetic energy is obtained by test filtering the resolved-scale velocity data:

$$q^2 = \tfrac{1}{2}(\tilde{u}_k - \hat{\tilde{u}}_k)^2 \tag{3}$$

The blending function Γ is based on the ratio of the wall distance d to a modeled form of the Taylor microscale:

$$\Gamma = \frac{1}{2}\left(1 - \tanh\left[5\left(\frac{\kappa}{\sqrt{C_\mu}}\eta^2 - 1\right) + \phi\right]\right) \quad \text{and} \quad \eta = \frac{d}{\alpha\chi} \tag{4}$$

where ϕ is set to $\tanh^{-1}(0.98)$ to fix the balancing position (where $\kappa\eta^2 = \sqrt{C_\mu}$) to $\Gamma = 0.99$, and the Taylor microscale is defined as $\chi = \sqrt{\nu/C_\mu\omega}$. The constant α is chosen to enforce the average RANS-to-LES transition ($\Gamma = 0.99$ position) for equilibrium boundary layers at the point where the wake law starts to deviate from the log law. To determine α for a particular inflow boundary layer, the following procedure is used [3]. First, a prediction of the equilibrium boundary layer is obtained, given freestream properties, a specified wall condition (adiabatic or isothermal) and a value for the boundary-layer thickness, from Coles' law of the wall/wake along with the van Driest transformation:

$$\frac{u_{\text{vd}}}{u_\tau} = \frac{1}{\kappa}\ell_n(d_w^+) + C + 2\frac{\Pi}{\kappa}\sin^2\left(\frac{\pi}{2}\frac{d}{\delta}\right) \quad \text{and} \quad d_w^+ = \frac{u_\tau d}{\nu_w} \tag{5}$$

with

$$u_{\text{vd}} = \frac{u_\infty}{A}\left\{\sin^{-1}\left[\frac{2A^2 u/u_\infty - B}{\sqrt{B^2+4A^2}}\right] + \sin^{-1}\left[\frac{B}{\sqrt{B^2+4A^2}}\right]\right\} \tag{6}$$

$$A = \sqrt{\frac{(\gamma-1)}{2} Pr_t M_\infty^2 \frac{T_\infty}{T_w}} \quad \text{and}$$
$$B = \left[1 + Pr_t^{1/2}\frac{(\gamma-1)}{2}M_\infty^2\right]\frac{T_\infty}{T_w} - 1 \tag{7}$$

An initial estimate for the outer extent of the log layer is defined by finding the value of d_w^+ such that

$$\left(\frac{1}{\kappa}\ell_n(d_w^+) + C\right) \Big/ \left(\frac{u_{\text{vd}}}{u_\tau}\right) = 0.98 \tag{8}$$

The value of $d^+ = u_\tau d/\nu$ that corresponds to this value of d_w^+ is then found through the use of Walz's formula for the static temperature distribution within the boundary layer:

$$\frac{T}{T_\infty} = \frac{T_w}{T_\infty} + \frac{(T_{aw} - T_w)}{T_\infty}\frac{u}{u_\infty} - r\frac{(\gamma-1)}{2}M_\infty^2\left(\frac{u}{u_\infty}\right)^2 \tag{9}$$

The model constant is then found by the equivalence $d^+ = \alpha^2$, which arises from the use of inner layer scaling arguments for k and ω. It should be noted that this approach is not universal, as the wake law is not universal. Reynolds-number effects, freestream pressure gradients, and surface curvature, for example, can all influence the shape of the wake region and the location at which it deviates from the logarithmic region. In this investigation, we use a spatially varying form of the model constant $\alpha = \alpha(x)$ by applying the above procedure to the boundary-layer thickness distribution as determined by a RANS simulation.

B. Interface Flux Reconstruction

We consider two methods for extending the baseline first-order upwind method [16] to higher order in this study. The baseline scheme is the piecewise parabolic method (PPM) [18], which reduces to a fourth-order approximation to the interface flux:

$$F_{i+1/2} = F_{i+1/2}(\mathbf{V}_{L,i+1/2}, \mathbf{V}_{R,i+1/2}) \tag{10}$$

with

$$\mathbf{V}_{L,i+1/2} = \mathbf{V}_{R,i+1/2} = \frac{7}{12}(\mathbf{V}_i + \mathbf{V}_{i+1}) - \frac{1}{12}(\mathbf{V}_{i+2} + \mathbf{V}_{i-1}) \tag{11}$$

if the data are sufficiently smooth. The PPM enforces local monotonicity by resetting left- and right-state values if local extrema

are detected. Specifically, the following limiting procedure is performed:

$$\begin{aligned}
&\text{if } \mathrm{sgn}[(\mathbf{V}_{L,i+1/2}-\mathbf{V}_i)(\mathbf{V}_i-\mathbf{V}_{R,i-1/2})]=-1, \quad \text{then}\\
&\quad \mathbf{V}_{L,i+1/2}=\mathbf{V}_{R,i-1/2}=\mathbf{V}_i\\
&\text{else}\\
&\quad C=\mathbf{V}_{L,i+1/2}-\mathbf{V}_{R,i-1/2}; \qquad D=6\left[\mathbf{V}_i-\frac{1}{2}(\mathbf{V}_{L,i+1/2}+\mathbf{V}_{R,i-1/2})\right]\\
&\quad \text{if } (DC>CC) \quad \text{then } \mathbf{V}_{R,i-1/2}=3\mathbf{V}_i-2\mathbf{V}_{L,i+1/2}\\
&\quad \text{elseif } (-CC>DC) \quad \text{then } \mathbf{V}_{L,i+1/2}=3\mathbf{V}_i-2\mathbf{V}_{R,i-1/2}\\
&\quad \text{end if}\\
&\text{end if}
\end{aligned} \tag{12}$$

The first "if" block in Eq. (12) resets the interpolation function to a constant if $\mathbf{V}_i$ is a local maximum or minimum. The second "if" block in Eq. (12) resets either the left-state value at interface $i+1/2$ or the right-state value at interface $i-1/2$ so that the interpolation parabola that connects the interface states with the state at the cell center is monotonically increasing or decreasing. It is also possible to enforce physical constraints (such as positive pressures and densities) at the cell interfaces by a similar cell-by-cell resetting algorithm. We also test the use of fifth order upwind-biased interpolations as a replacement for Eq. (11):

$$\begin{aligned}
\mathbf{V}_{L,i+1/2}&=\frac{2}{60}\mathbf{V}_{i-2}-\frac{13}{60}\mathbf{V}_{i-1}+\frac{47}{60}\mathbf{V}_i+\frac{27}{60}\mathbf{V}_{i+1}-\frac{3}{60}\mathbf{V}_{i+2}\\
\mathbf{V}_{R,i+1/2}&=-\frac{3}{60}\mathbf{V}_{i-1}+\frac{27}{60}\mathbf{V}_i+\frac{47}{60}\mathbf{V}_{i+1}-\frac{13}{60}\mathbf{V}_{i+2}+\frac{2}{60}\mathbf{V}_{i+3}
\end{aligned} \tag{13}$$

We also consider different choices for the variable vector used in the reconstruction: $\mathbf{V}=[\rho,u,v,w,T,k,\omega]^T$ and $\mathbf{V}=[p,u,v,w,T,k,\omega]^T$. In the discussion that follows, the use of the first set of variables will be denoted as SCHEME(ρ,T) (SCHEME being PPM4 or PPM5), while the second is denoted as SCHEME(p,T). The PPM requires a seven point stencil in each coordinate direction for both the fourth- and fifth-order variants.

C. Inflow Generation Methods

A key element of the hybrid LES/RANS formulation is the use of recycling/rescaling techniques to initiate and sustain grid-resolved turbulent structures in the outer part of the boundary layer. Among recycling/rescaling techniques recently proposed in the literature for compressible flows [3,6,8–11], we consider three variants in the present study. In the first method, the recycled and rescaled velocity, temperature, and density fluctuations are imposed onto the RANS mean inflow [3,6]. The density fluctuations are adjusted so that a specified rms value (2% in this work) for the pressure fluctuations is maintained, and the temperature fluctuations are also scaled so that Morkovin's hypothesis is not violated [3]. In the second method, we separately recycle and rescale the mean and fluctuating velocity and temperature fields. The density field is obtained by enforcing a constant-pressure condition at the inflow [8]. In the third approach, recycled and rescaled mean and fluctuating density fields are also imposed as inflow conditions without assuming that the pressure remains constant [9].

The current technique also includes an intermittency function for preventing recycled fluctuations from affecting the freestream regions and in some cases, from accumulating too much energy in the outer part of the boundary layer. In this, recycled and rescaled fluctuations are multiplied by a Klebanoff-type intermittency function [19]:

$$\Gamma_{\mathrm{kleb}}(d)=(1+(d/C_{\mathrm{kleb}}\delta_{\mathrm{in}})^6)^{-1} \tag{14}$$

where C_{kleb} is a model constant and δ_{in} is the inflow boundary-layer thickness, before being added to the mean profile. Our baseline value for C_{kleb} is 1.1; other choices for C_{kleb} are considered in the present study. Turbulence variables (k,ω,Γ) are recycled and rescaled without decomposing them into mean and fluctuating components [3]. Details are given in the Appendix.

D. Computational Details

Three different high Reynolds-number flows developing on flat plates are considered in the present study. For each case, the boundary-layer properties corresponding to the reference experiments are shown in Table 1. The Reynolds numbers (based on the boundary-layer thickness) range from 5.59×10^4 to 1.58×10^6. The incoming Mach number ranges from 2.32 to 2.80. Mean-flow and second-moment data for these boundary layers have been reported in [12–14,20–23]. Based on the thickness (δ_0) of the boundary layer at the measurement station, the sizes of the computational domain are $10\delta_0$, $5\delta_0$, and $6.4\delta_0$ in streamwise, wall-normal, and spanwise directions, respectively. The baseline meshes are generated so that approximately 20 uniformly spaced cells per incoming boundary-layer thickness are present in the streamwise and spanwise directions, and each mesh contains $200\times128\times200$ cells (5.12×10^6) in the streamwise, spanwise, and wall-normal directions, respectively. The grids are clustered to the surface in the wall-normal direction using a hyperbolic tangent stretching function so that the minimum grid spacing in wall units is less than 1.

The incoming boundary layer is generated by using the recycling/rescaling methods described in the previous section. The recycling station is located at $7.5\delta_0$ downstream of the inlet. Supersonic outflow boundary conditions are used at the far field and outlet, while a no-slip boundary condition is used at the wall. A constant wall temperature of 276 K is specified for the Smits and Muck [14] case, in accord with published information on this experiment, while an adiabatic wall condition is used for the other cases. Periodic boundary conditions are used in the spanwise direction. The initial condition is a RANS 2-D flat-plate solution, to which a rescaled fluctuation field from an earlier calculation is superimposed [3]. Following a period of about five flow-through times to remove initial transients, time- and span-averaged statistics are collected over a minimum of 10 flow-through times ($100\delta_0/U_\infty$). The computational time step ranged from 0.25–0.4 μs, with the differences in time step being related to variations in the mesh sizes discussed later.

III. Assessment of the Hybrid LES/RANS Method

If the LES/RANS model of Edwards et al. [3] operates as designed, the outer layer will be computed as a large-eddy simulation and will force the development of the inner layer so that a uniform boundary-layer structure will emerge in the time and span average. The sensitivity of this response to various factors should be determined, however, to understand the limitations of the approach and to establish practices that consistently lead to acceptable boundary-layer predictions. For this purpose, we characterize the effect of modeling and algorithm parameters on turbulent statistics through comparisons with experimental data of Luker et al. [12].

Table 1 Turbulent boundary-layer properties for the referenced experiments

Case	M_∞	δ_0, mm	U_∞, m/s	Re_δ	P_o, pa	T_o, K	Ref. experiment
E0	2.32	10 (12) [a]	552	5.59×10^4	5.0×10^4	291	Elena and Lacharme [13]
L0	2.80	9.9	602	1.78×10^5	2.1×10^5	298	Luker et al. [12]
S0	2.79	25	562	1.58×10^6	6.9×10^6	263	Smits and Muck [14]

[a]Note that * is based on 99.9% of freestream velocity.

Table 2 Numerical parameters of the present hybrid LES/RANS simulations

Case	α	C_{kleb}	Recon. variables	Scheme	δ/Δ	Inflow method
L0	α_0	1.1	p, T	PPM4	20	Edwards et al. [3]
L1	α_m	1.1	p, T	PPM4	20	Edwards et al. [3]
L2	α_0	2.0	p, T	PPM4	20	Edwards et al. [3]
L3	α_0	∞	p, T	PPM4	20	Edwards et al. [3]
L4	α_0	1.1	ρ, T	PPM4	20	Edwards et al. [3]
L5	α_0	1.1	p, T	PPM5	20	Edwards et al. [3]
L6	α_0	1.1	p, T	PPM4	10	Edwards et al. [3]
L7	α_0	1.1	p, T	PPM4	30	Edwards et al. [3]
L8	α_0	1.1	p, T	PPM4	10	Urbin and Knight [8]
L9	α_0	1.1	p, T	PPM4	10	Stolz and Adams [9]
E0	α_0	1.1	p, T	PPM4	20	Edwards et al. [3]
S0	α_0	1.1	p, T	PPM4	20	Edwards et al. [3]

In that reference, experimental uncertainties for the velocity measurements are estimated to range between 1.3 and 3.3% of the freestream velocity, depending on the location within the boundary layer. Experimental uncertainties for the rms fluctuation intensities range between 0.08 and 0.26% of the freestream velocity, and uncertainties for the Reynolds-shear stresses ($\overline{u'v'}$) range between 0.002 and 0.029% of the square of the freestream velocity. Table 2 shows the numerical parameters for the cases computed as part of this assessment as well as those for the Elena and Lacharme [13] and Smits and Muck [14] experiments. Note that the characters L, E, and S represent the Luker et al. [12], Elena and Lacharme [13], and Smits and Muck [14] experiments, respectively. Predictions at the target location are compared with mean-flow velocity profiles and Reynolds-stress measurements from the references. Reynolds shear-stress predictions are normalized by the wall shear stress at the measurement location, whereas Reynolds streamwise and wall-normal stresses are presented as rms fluctuation intensities u'_{rms} and v'_{rms}, which are normalized by the edge velocity. Distances from the wall are normalized by the target (experimental) boundary-layer thickness so that the ability of the methods to predict the growth rate of the boundary layer can be assessed more clearly. Velocities are normalized by the predicted edge velocity.

A. Effect of Model Constant for LES/RANS Transition

First, we focus on the effect of model constant α, which shifts the target position of the midpoint of the LES/RANS transition region. The procedure in Sec. II.A, when applied to the 2-D flat-plate boundary layer as predicted by the RANS model, gives a spatially varying constant that may be regressed as a linear distribution $\alpha(x) = 22.276 + 0.145(x/\delta_0)$. This distribution is used as the baseline and is designated as $\alpha_0(x)$. This choice is designed to force the time-averaged LES/RANS transition to occur at the point where the wake law just begins to depart from the logarithmic law. With this

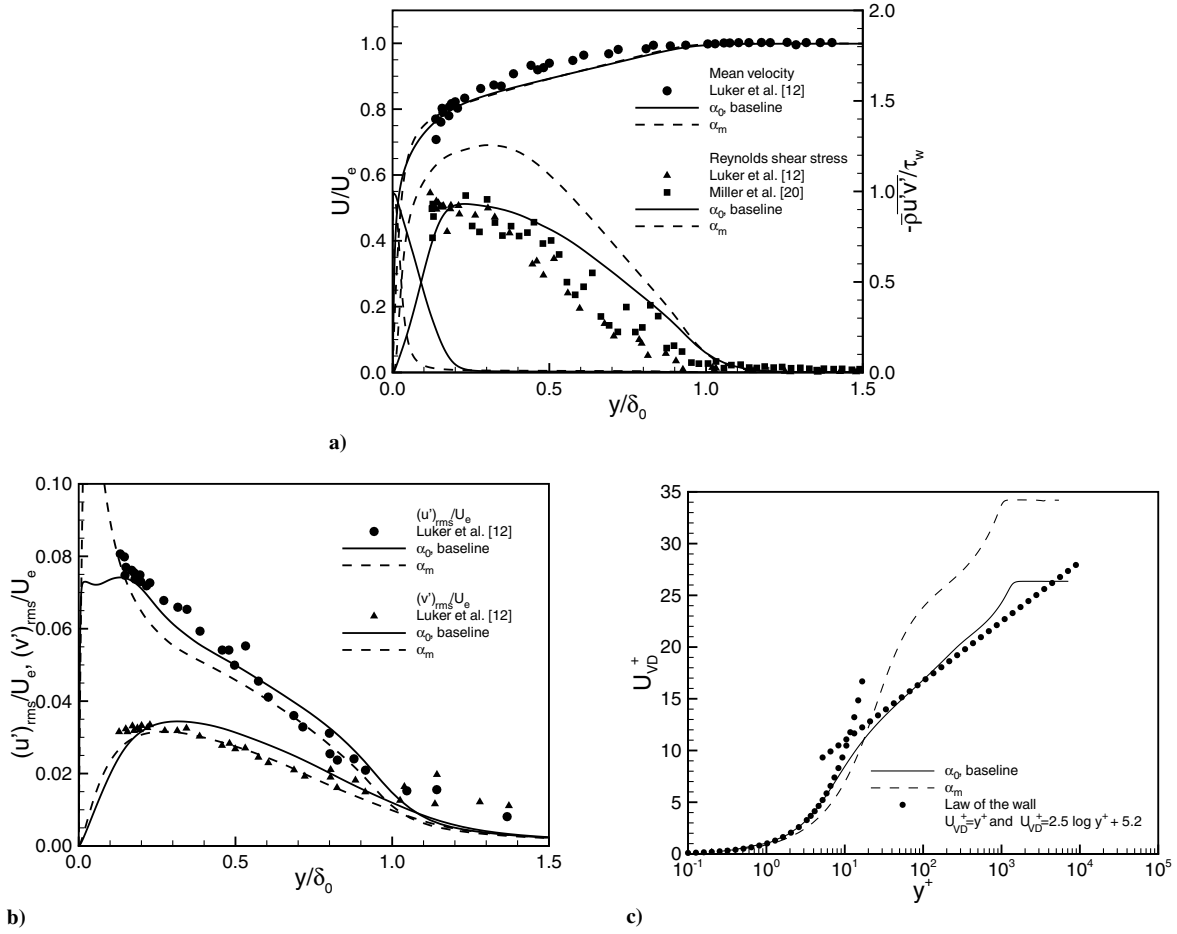

Fig. 1 Effect of model constant α on a) mean velocity profiles and Reynolds-shear stress predictions, b) streamwise and wall-normal Reynolds-stress predictions, and c) velocity profiles in wall coordinates.

choice, the entire logarithmic region is heavily influenced by the RANS closure even though some turbulence structure and significant unsteadiness is still present. Another possible choice of the model constant is to use the midpoint of the logarithmic layer as the average transition location. A regression equation for the second choice is $\alpha_m(x) = 12.771 + 0.036(x/\delta_0)$. Figure 1 compares the mean velocity profile and Reynolds stresses obtained using the baseline $\alpha_0(x)$ distribution and the $\alpha_m(x)$ distribution. Other modeling parameters are given in Table 2. The predictions obtained using the baseline distribution $\alpha_0(x)$ are in good agreement with experimental results (Fig. 1a), while the second choice $\alpha_m(x)$ leads to an overly energetic near-wall velocity profile (Fig. 1c). The Reynolds-shear stresses are overpredicted in the entire boundary layer for the $\alpha_m(x)$ distribution (Fig. 1a), reaching values well in excess of the wall shear stress, but the predictions of the Reynolds normal stresses in the near-wall region show slightly better agreement with experimental results when the $\alpha_m(x)$ distribution is used. In Fig. 1a and in subsequent ones, the modeled component of the Reynolds-shear stress is indicated toward the left axis ($y/\delta_0 \to 0$). The modeled component decays nearly to zero through the action of the blending function (though a subgrid component remains) and is supplanted by the resolved Reynolds stress in the outer layer. The total Reynolds stress can be estimated by summing the modeled and resolved components. The modeled components of the Reynolds normal stresses are neglected in Fig. 1b and in subsequent ones. In our code, we absorb the trace of the modeled Reynolds-stress tensor into the effective pressure. The remaining normal-stress components are very small in the near-wall region when the Boussinesq hypothesis is invoked, and as such, high accuracy in normal-stress predictions near the surface cannot be expected. The boundary-layer thickness as indicated by the Reynolds-stress measurements is overpredicted for both cases. This example shows that a precise embedding of the RANS component of the LES/RANS model is a critical factor in achieving accurate turbulent statistics for very high Reynolds-number flows.

B. Effect of Interface Flux Reconstruction

Years of experience with DNS and LES methods have shown that higher order, minimally dissipative numerical methods with high bandwidth efficiency are required to sustain turbulent eddy

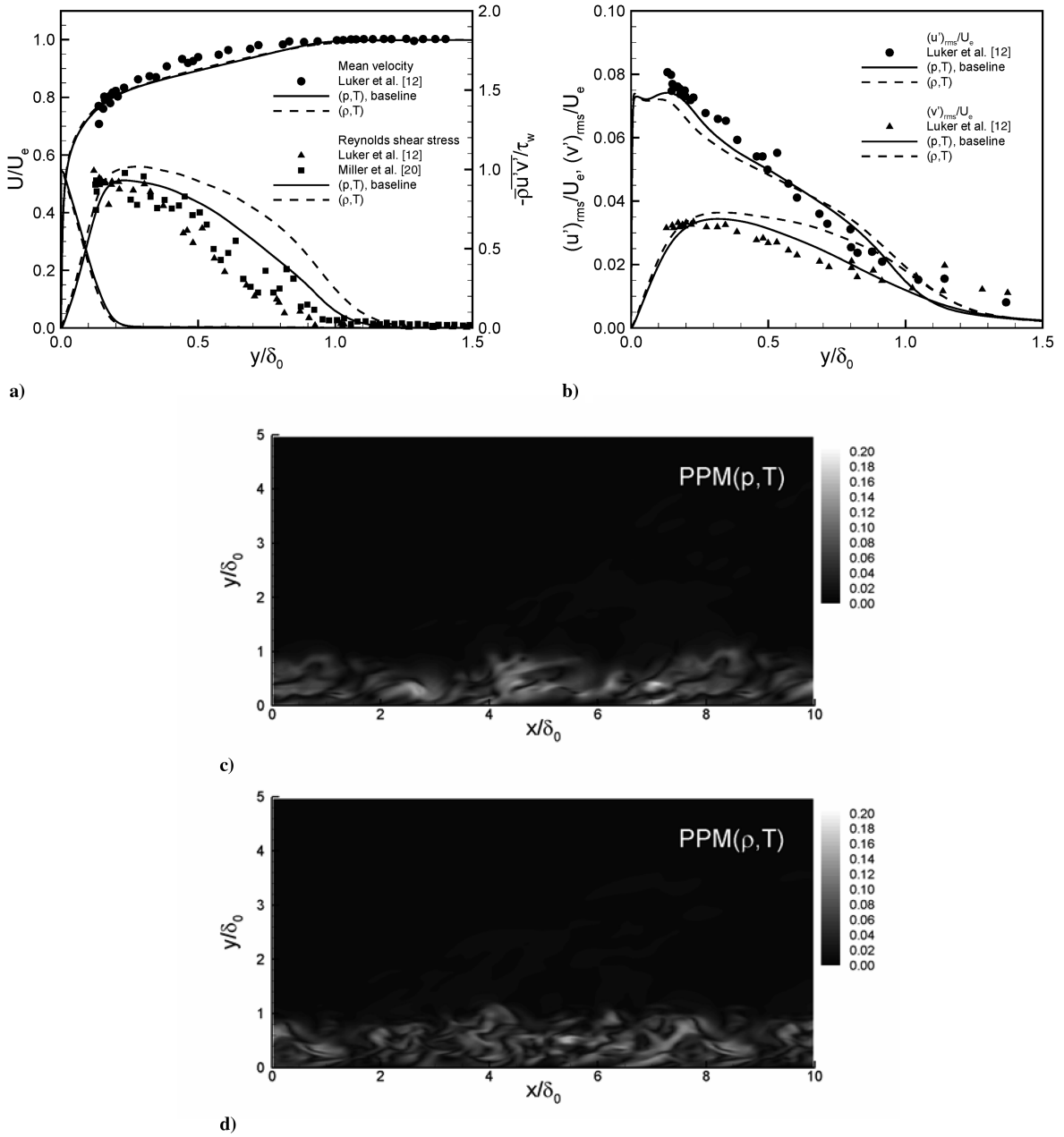

Fig. 2 Effect of reconstruction variables on a) mean velocity profiles and Reynolds-shear stress predictions, b) streamwise and wall-normal Reynolds-stress predictions, c) transverse-velocity magnitude snapshots of PPM4(p, T), and d) of PPM4(ρ, T).

structures. When shocks are considered, then it becomes more difficult to meet these requirements, as they conflict with the need to maintain monotone capturing of discontinuities to avoid numerical instabilities. We consider two aspects of the reconstruction procedure in the context of the baseline PPM scheme presented in Sec. II.B. The effects of the choice of the variable vector [PPM4(ρ, T) or PPM4(p, T)] used in the reconstruction are shown in Fig. 2. Other modeling parameters are the same as those of the baseline case. The shape of the mean velocity profile is not very sensitive to this choice, whereas the levels of Reynolds-shear and wall-normal stresses are increased significantly in the outer part of the boundary layer for the PPM4(ρ, T) reconstruction, relative to that provided by the PPM4(p, T) reconstruction. This might be explained by the following two factors. First, the interface pressure, for the PPM4(ρ, T) reconstruction, will be obtained as a product of the interface density and temperature. The difference in the pressure gradient as calculated from this formulation and that obtained directly from the PPM4(p, T) reconstruction can be interpreted as a blend of diffusive and antidiffusive terms, and it is possible that these additional transport mechanisms give rise to the amplification of transverse-velocity components. Another factor is that the PPM limiting procedure may act more strongly on the pressure than it does on the density and temperature. This could mean that grid-scale noise in the pressure field is damped more strongly in the PPM4(p, T) reconstruction, leading to a suppression of similar noise in the transverse-velocity components. More smaller-scale structures are captured for PPM4(ρ, T), particularly toward the outer part of the boundary layer, as shown in the transverse-velocity magnitude snapshots of Figs. 2c and 2d. The energy contained in these structures appears to be in excess of that expected, based on the comparisons with experimental data, and this behavior can lead to unphysical levels of boundary-layer growth if the spatial domain is long enough.

Next, we compare two different variable-extrapolation techniques, PPM4(p, T) and PPM5(p, T), for the reconstruction of the fluid properties at the interface. The PPM4 scheme can be viewed as a central-differencing scheme that is stabilized through the local use of monotonicity-preserving techniques. Such schemes may be subject to aliasing due to the nonlinearity inherent in the flux functions. The fifth-order, upwind-biased extrapolations used in PPM5 should be less susceptible to aliasing effects. Figure 3 shows that there are no essential differences in the predictions of the mean velocity profile and second-moment quantities provided by PPM4(p, T) and PPM5(p, T).

C. Effect of Inflow Generation Method

The effects of the three inflow generation methods described in Sec. II.C are described in this section. The interface fluxes are reconstructed by PPM4(p, T), the baseline model-constant distribution $\alpha_0(x)$ is used, and the constant C_{kleb} in the intermittency function is set to 1.1. Figure 4 illustrates the effect of the Urbin and Knight procedure [8] for rescaling the mean inflow profile as compared with the use of a RANS inflow profile [3] and the Stolz and Adams procedure [9]. The results indicate that rescaling the mean and fluctuating fields using the Stolz and Adams procedure [9] yields slightly better predictions for the mean velocity profile, particularly in the inner region. The resolved Reynolds stresses for all cases fall within the data ranges of the experiments. In detail, some differences in Reynolds-shear stresses are observed in the inner region, while no significant difference is found in the outer region. The predictions of

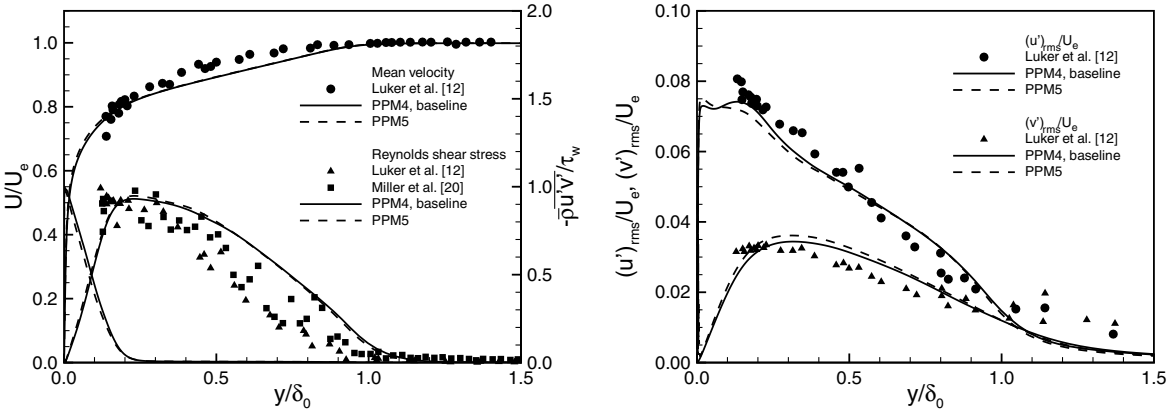

a) b)

Fig. 3 Effect of reconstruction method on a) mean velocity profiles and Reynolds-shear stress predictions, and b) streamwise and wall-normal Reynolds-stress predictions.

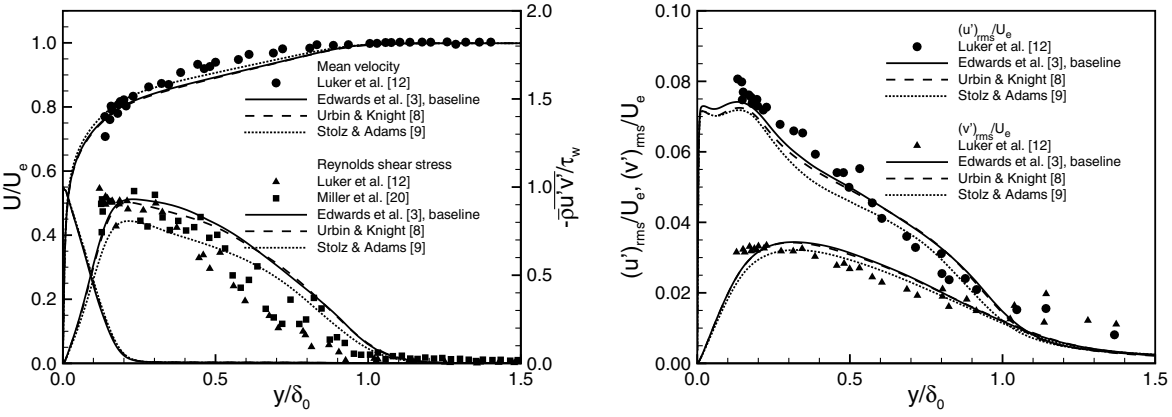

a) b)

Fig. 4 Effect of inflow method on a) mean velocity profiles and Reynolds-shear stress predictions, and b) streamwise and wall-normal Reynolds-stress predictions.

the Reynolds normal stresses show no significant difference among the methods. All cases show that the boundary-layer thickness at the target location is overestimated, with this quantity being reduced slightly when the fixed RANS mean inflow is used. All methods result in a transition region near the inlet (extending $\sim 3\delta_0$ downstream) [9] where the flow attempts to adjust to the imposed inflow condition through the generation of various compression/expansion waves. The growth of the boundary layer is delayed in this transition region until these waves are attenuated.

To prevent recycled fluctuations from affecting the freestream regions, we use a Klebanoff-type intermittency function to damp recycled fluctuations [Eq. (14)]. The extent of the intermittency function is controlled by the model constant C_{kleb}. Figure 5 shows the effect of C_{kleb} on the mean velocity profile and Reynolds-stress distributions. Increasing C_{kleb} allows more amplification of turbulent fluctuations in the outer region, leading to more growth of the boundary layer. The shapes of the profiles do not change significantly except near the outer edge of the boundary layer, where the wake region expands in accord with the increase in C_{kleb}. The choice of $C_{\text{kleb}} = 1.1$ provides better predictions based on the experimental results. Recently, Sagaut et al. [11] reported that existing inflow generation methods cannot sustain target values for boundary-layer integral properties over long integration times, and this observation is confirmed in our work. The intermittency function appears to help maintain a target boundary-layer thickness while also isolating the freestream region from being affected by the recycling procedure.

D. Effect of Spatial Resolution

The spatial resolution in the wall-transverse directions (streamwise and spanwise directions) is also expected to influence predictions of the boundary-layer structure. For the hybrid LES/RANS methods, the mesh should be generated so that the outer layer is resolved adequately. We use the Escudier mixing length ($\sim 0.1\delta_0$) [19] as an upper bound for the mesh spacing and choose half of this value as the baseline mesh spacing ($\delta/\Delta = 20$). To examine the effects of mesh resolution on the predicted quantities, we consider three levels of mesh refinement (10 cells/δ_0, 20 cells/δ_0, and 30 cells/δ_0) as shown in Table 2. Figure 6 shows that the mean velocity profile and Reynolds stresses for the baseline grid simulation are in good agreement with those for the fine-grid simulation. The wall-normal Reynolds stress and the resolved Reynolds-shear stress are underpredicted for the coarse-mesh simulation. The underprediction of the resolved Reynolds-shear stress is partially compensated for by an increase in the modeled Reynolds-shear stress, and as such, the mean velocity profile is relatively unaffected by the mesh resolution. This result is encouraging as it indicates that acceptable results might be obtained on marginally resolved meshes for the present hybrid LES/RANS technique.

IV. Compressible Boundary-Layer Flows at High Reynolds Numbers

Using the baseline parameters [PPM4(p,T), $C_{\text{kleb}} = 1.1$, Edwards et al.'s recycling/rescaling [3], 20 cells/δ_0], we apply the method to experiments [13,14] conducted at Reynolds numbers lower and higher than the baseline [12] to test the Reynolds-number independence of the present model and to illustrate the effect of the Reynolds number on the mean and instantaneous turbulent flow structure. The boundary-layer properties for each

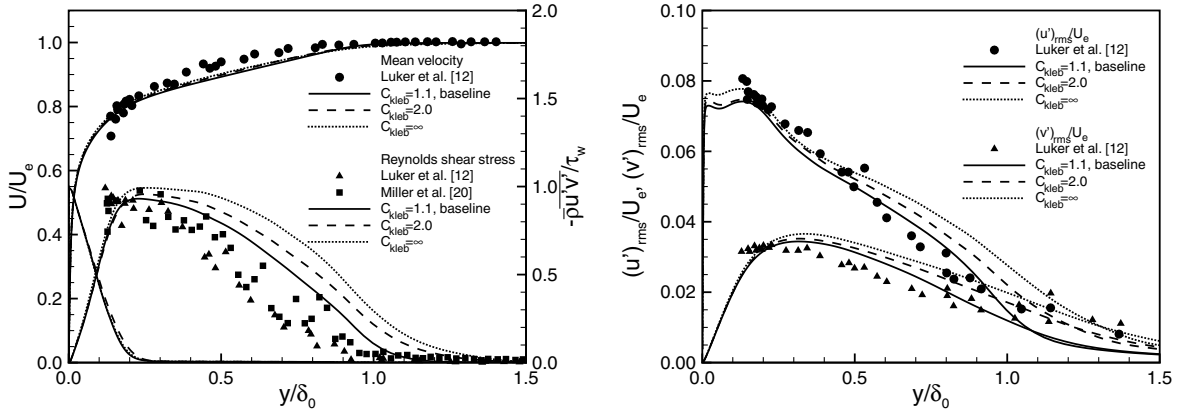

Fig. 5 Effect of model constant C_{kleb} on a) mean velocity profiles and Reynolds-shear stress predictions, and b) streamwise and wall-normal Reynolds-stress predictions.

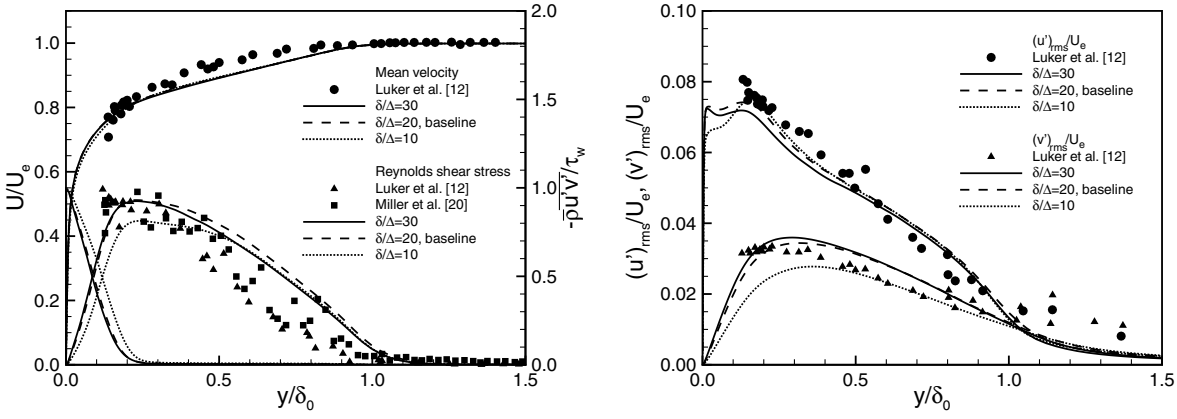

Fig. 6 Effect of streamwise and spanwise grid size on a) mean velocity profiles and Reynolds-shear stress predictions, and b) streamwise and wall-normal Reynolds-stress predictions.

case are listed in Table 1 and the corresponding numerical parameters are shown in Table 2.

A. Mean Velocity and Reynolds Stress

Figure 7 compares results from the hybrid LES/RANS computations with hot-wire and laser Doppler anemometer (LDA) measurements reported by Elena and Lacharme [13]. Experimental uncertainty estimates [13] range from 0.06 to 0.66% for mean velocity ($\Delta u/u$), from 4.7 to 10% for rms velocity fluctuations ($\Delta\sqrt{\bar{u}'^2}/\bar{u}'^2$), and less than 30% for Reynolds-shear stress ($\Delta\overline{u'v'}/\overline{u'v'}$). The regression equation for the model constant α is extracted from a prior RANS computation: $\alpha(x) = 13.409 + 0.100(x/\delta_0)$. The results show good agreement with the experimental data. Compared to recent DNS data of this case [24], the Reynolds stresses are comparable in the outer part of the boundary layer but differ near the wall due to the presence of the RANS component in the turbulence closure. Figure 8 shows mean velocity profile and Reynolds-stress predictions for the present method as applied to the Smits and Muck [14] experiment. Experimental uncertainty estimates [14] for rms mass-flux fluctuation and Reynolds-shear stress measurements are reported as -5 to $+9\%$ for the former and -27 to $+11\%$ for the latter. A regression equation $\alpha(x) = 72.389 + 0.356(x/\delta_0)$ from the initial RANS computation is used. Good agreement with the experimental data is evidenced, though the wall-normal Reynolds stress is slightly underpredicted. The results shown in Figs. 1, 7, and 8 indicate that the present hybrid LES/RANS method is able to provide a degree of Reynolds-number independence in the predictions of the boundary-layer structure.

Figure 9 plots van Driest-transformed velocity profiles for the different Reynolds-number cases. As expected, the extent of the logarithmic layer increases with the increase in Reynolds number. Figure 10 shows the effect of Reynolds number on the Reynolds stresses. The wall-normal coordinate is normalized by the predicted boundary-layer thickness at the $7.5\delta_0$ location. The peak positions of the Reynolds stresses move away from the wall as the Reynolds number increases. This might be related to the effect of the RANS closure. In the outer layer, there is no significant variation in the Reynolds-stress distributions with respect to Reynolds number. These results indicate that, given similar Mach numbers [25], the outer layer scaling of the turbulent statistics has no dominant dependence on Reynolds number, similar to observations in incompressible flows [26].

B. Boundary-Layer Properties

The time-averaged skin-friction coefficient C_f is determined from the averaged streamwise velocity and the molecular viscosity computed according to Sutherland's law using the time-averaged temperature [25]. Figure 11a shows a comparison of the present C_f with several experimental results [12,13,21,27–30] as a function of Reynolds number based on momentum thickness. Variations of C_f in the computational domain are marked as error bars. A theoretical prediction of the skin-friction variation for incompressible flows [26] is also shown in the figure. The present results are in good agreement with a regression (based on power law) of the experimental data. Figure 11b shows the time-averaged streamwise evolution of the boundary thickness for the different Reynolds-number cases.

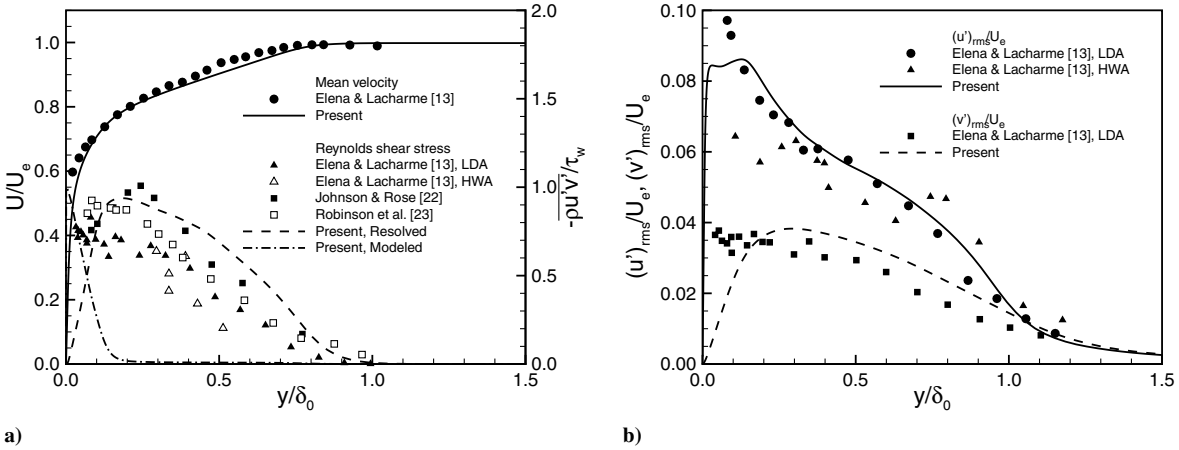

a) b)

Fig. 7 a) Mean velocity profiles and Reynolds-shear stress predictions, and b) streamwise and wall-normal Reynolds-stress predictions for the Elena and Lacharme [13] case. HWA stands for hot-wire anemometer.

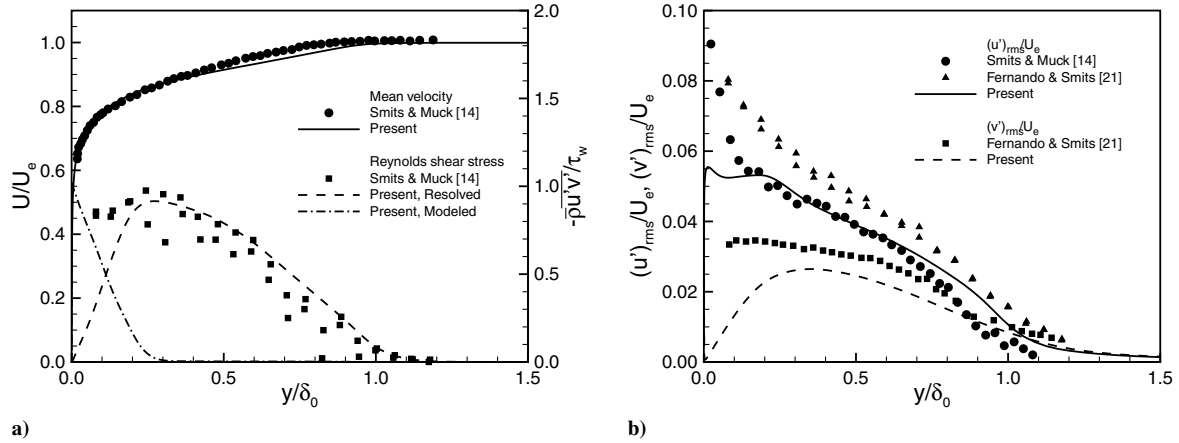

a) b)

Fig. 8 a) Mean velocity profiles and Reynolds-shear stress predictions, and b) streamwise and wall-normal Reynolds-stress predictions for the Smits and Muck [14] case.

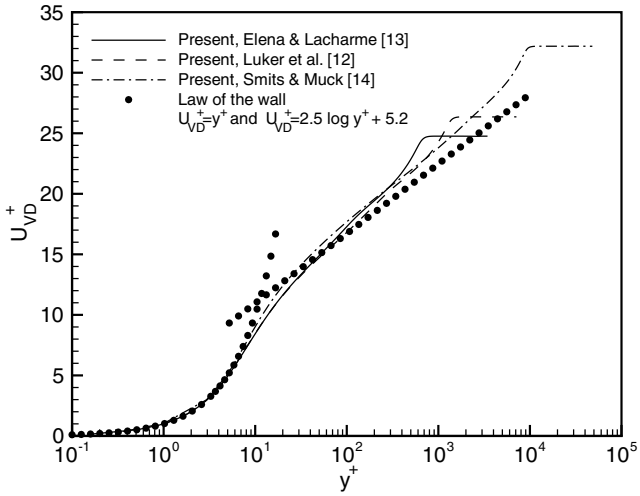

Fig. 9 Mean velocity profiles for the present hybrid LES/RANS simulations of three different Reynolds-number flows.

Empirical correlations based on power-law relations for the boundary-layer integral parameters [25] are also shown in the figure. The growth rates of the boundary layer in the correlations are readjusted to the incoming boundary-layer thickness used in the present simulations. The present growth rates indicate two distinct features. First, the initial growth rates for all cases are underestimated, relative to the empirical correlations. Secondly, after a transition region of $\sim 3\delta_0$ (discussed earlier), the boundary layer redevelops, and the corresponding growth rate maintains the empirical rates except for the case corresponding to Elena and Lacharme's experiment [13]. The predicted boundary-layer thicknesses at the target location are larger than the experimental values by 1 to 6%.

C. Swirl Strength

We visualize turbulent structures using the swirl strength λ_{ci} [31], which indicates the degree of coherence in the structures. The swirl strength is the imaginary part of the complex conjugate eigenvalue of the velocity gradient tensor. Figure 12 plots the swirl strength for the three boundary layers considered herein. The isosurfaces are based on a criterion that λ_{ci} equals to $2.5\bar{\lambda}_{ci}$, where $\bar{\lambda}_{ci}$ is the mean value for each boundary layer. To distinguish the vortical structures in the outer layer, structures in the range $y/\delta_0 < 0.2$ are excluded. The colors represent the levels of spanwise vorticity from -2 to 2. Several hairpinlike vortices are observed, and elongated structures in the streamwise direction are also clearly captured in all cases. Patterns of the structures show no significant differences among the cases, though some structures in the Elena and Lacharme [13] case reach a higher level of spanwise vorticity.

Figure 13a shows the mean values of the swirl strength as a function of wall-normal distance. The mean values are computed using 40 time realizations of the instantaneous flow field, separated

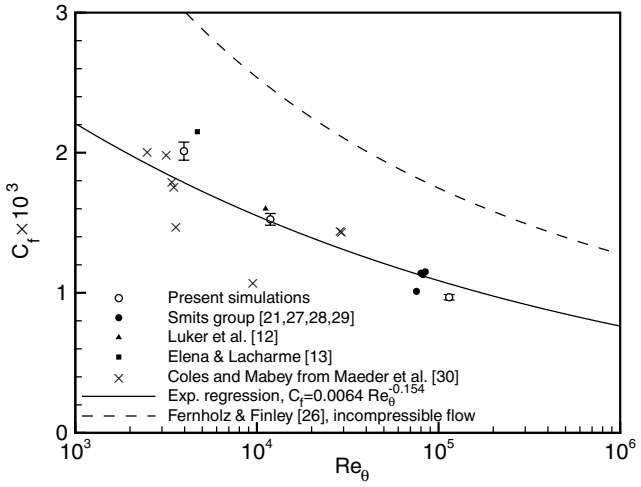

a)

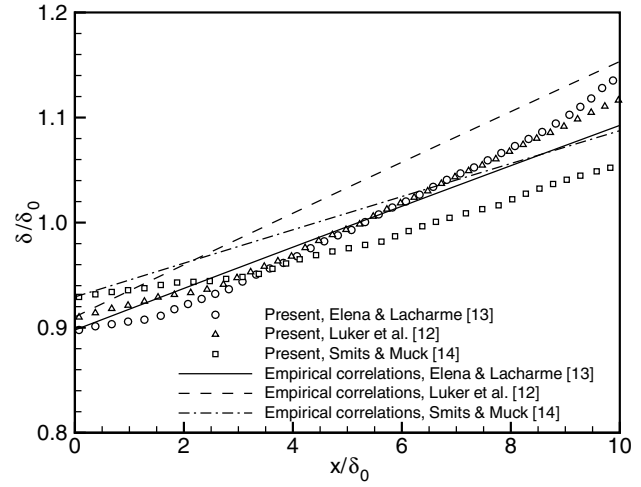

b)

Fig. 11 The effect of Reynolds number on a) skin-friction coefficient and b) boundary-layer growth rates.

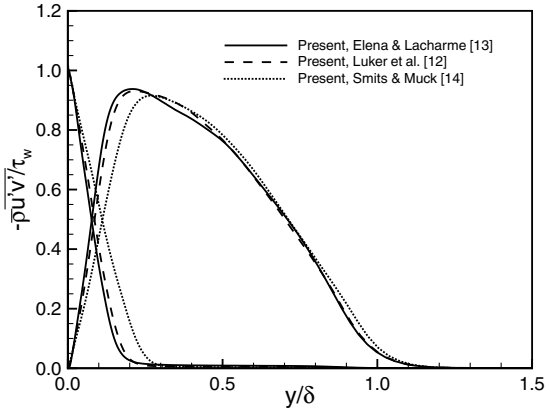

a)

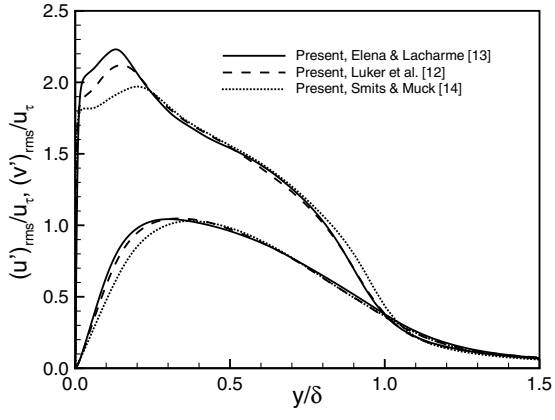

b)

Fig. 10 The effect of Reynolds number on a) Reynolds-shear stress and b) streamwise and wall-normal Reynolds-stress distributions.

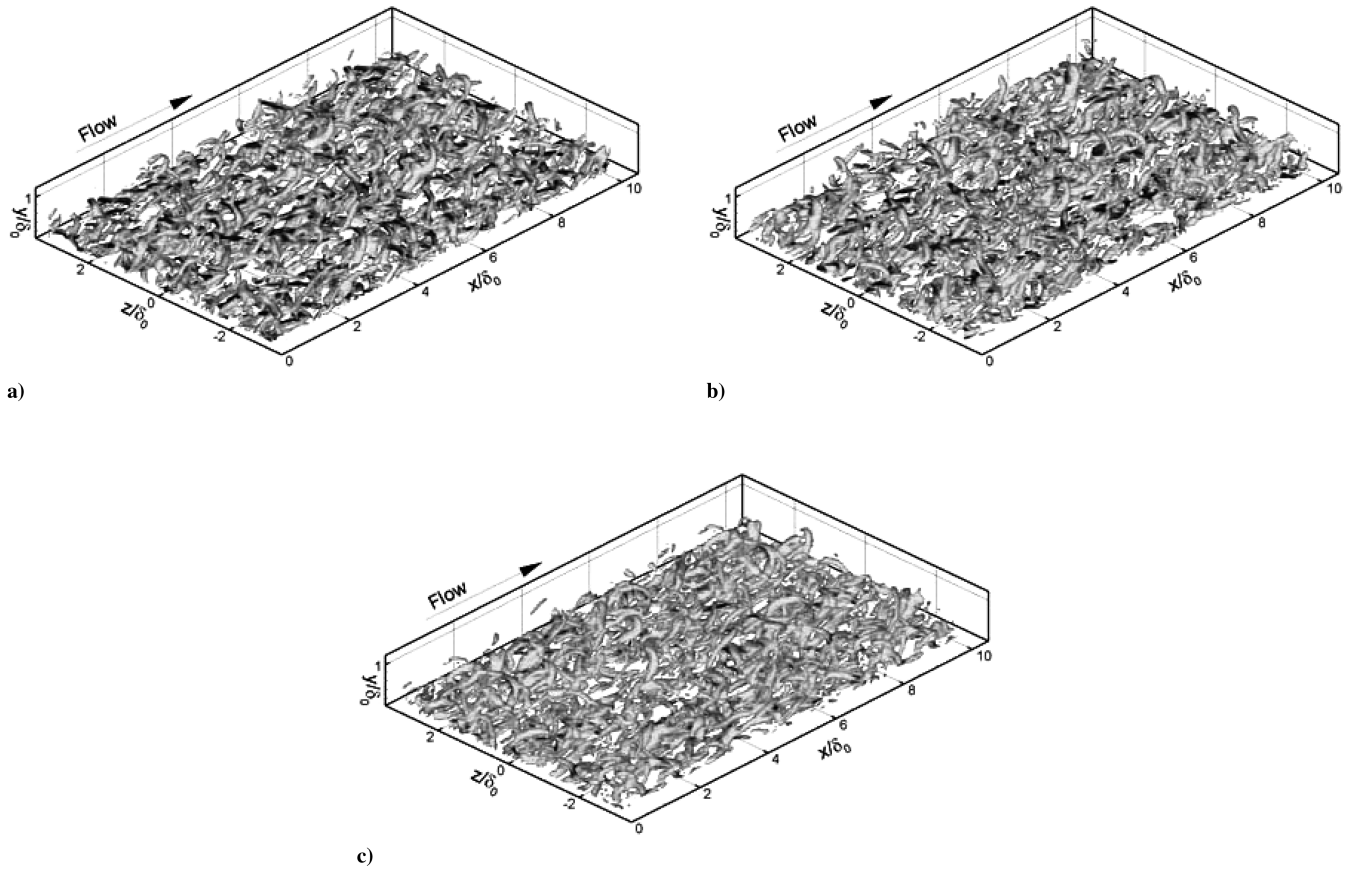

Fig. 12 Vortical structures visualized using an isosurface of $\lambda_{ci} = 2.5\bar{\lambda}_{ci}$ for three different Reynolds-number flows; a) the Elena and Lacharme [13] case; b) the Luker et al. [12] case; c) and the Smits and Muck [14] case.

by approximately $3.0\delta_0/U_\infty$. We use the data in a streamwise interval $4 \leq x/\delta_0 \leq 9$ to avoid the initial transient effects discussed in the previous section. The swirl strength is normalized as $\lambda^*_{ci} = \lambda_{ci}(\delta_0/u_\tau)$, considering a time scale δ_0/u_τ in the boundary layer. The swirl strength linearly decreases as the boundary-layer edge is approached, implying an increase in the turbulence time scale. In general, the decay rates of the mean swirling strength show no significant differences for the three different boundary layers. This implies that the evolution of the turbulent structures in the outer part of the boundary layer ($y/\delta_0 > 0.3$) is similar for the different cases. Peak values of the mean swirl strength are observed near $y/\delta_0 \approx 0.2$, where the resolved Reynolds-shear stresses are at their maximum, and the peak values decrease as the Reynolds number is increased. This reduction may be related to inadequate resolution in the buffer region and to the increase in the modeled component of the Reynolds stress as the Reynolds number increases. Figure 13b shows probability density functions $P(\lambda^*_{ci})$ of the normalized swirling strength. The probability density functions are computed by binning the swirl strength values in the entire boundary layer and then ensemble averaging:

$$P(\lambda^*_{ci}) = \frac{\langle \int_{\Omega_V} N(\lambda^*_{ci}) \mathrm{d}V \rangle}{\int \langle \int_{\Omega_V} N(\lambda^*_{ci}) \mathrm{d}V \rangle \mathrm{d}\lambda^*_{ci}} \tag{15}$$

where Ω_V is the interrogation domain, $\langle\,\rangle$ represents an ensemble average, and $N(\lambda^*_{ci})$ is a number of events in a bin representing λ^*_{ci}. The most probable values of the swirl strength are found near the location where $\log_{10}(\lambda^*_{ci})$ is approximately 0.8. This result also implies that the predominant (normalized) turbulence time scale in the outer layer does not strongly depend on the Reynolds number.

D. Velocity Correlations

Two-point correlations based on the streamwise velocity fluctuations (u') are determined to investigate their coherence. The streamwise–spanwise (R_{xz}) and streamwise–normal correlations (R_{xz} and R_{xy}) are defined as

$$R_{xz}(\Delta x, \Delta z; y_{\mathrm{ref}}) = \frac{\overline{u'(x, y_{\mathrm{ref}}, z) u'(x + \Delta x, y_{\mathrm{ref}}, z + \Delta z)}}{\sigma^2_{u'}(y_{\mathrm{ref}})} \tag{16}$$

$$R_{xy}(\Delta x, y; y_{\mathrm{ref}}) = \frac{\overline{u'(x, y_{\mathrm{ref}}, z) u'(x + \Delta x, y, z)}}{\sigma_{u'}(y_{\mathrm{ref}}) \sigma_{u'}(y)} \tag{17}$$

where Δx and Δz are the streamwise and spanwise separation distances, y_{ref} is the reference wall-normal location, $\sigma_{u'}$ is the rms of u', and the overbar indicates a spatial and ensemble average. The correlations are defined as $-2 \leq \Delta x/\delta_0 \leq 2$ and $-1 \leq \Delta z/\delta_0 \leq 1$ in the streamwise and spanwise directions, respectively.

Figure 14a shows streamwise–spanwise correlations (R_{xz}) for the Smits and Muck [14] case at four different reference locations, $y_{\mathrm{ref}}/\delta_0 = 0.3$, 0.5, 0.7, and 0.9, which span the outer part of the boundary layer. The contour levels range from -0.1 to 1.0 with increments of 0.1. Note that negative levels are marked by dashed lines and that the zero contour level is not shown. Elongated positive correlations neighbor elongated negative correlations in the streamwise direction at $y_{\mathrm{ref}}/\delta_0 = 0.3$. The streamwise length of the positive correlations ($R_{xz} = 0.1$) decreases but the spanwise length increases when the reference position is located farther away from the wall. Note that the streamwise length is at least 2 times larger than the spanwise length below $y_{\mathrm{ref}}/\delta_0 = 0.5$. Near the boundary edge, the structure tends to be more isotropic. This is consistent with the results of experiments [28,32]. Figure 14b shows streamwise–normal correlations (R_{xy}) at different reference locations. A forward-leaning structure which contains a significant spatial coherence in the

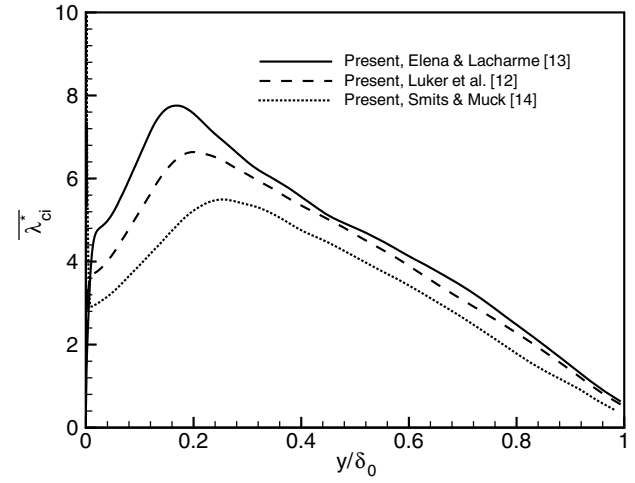

a)

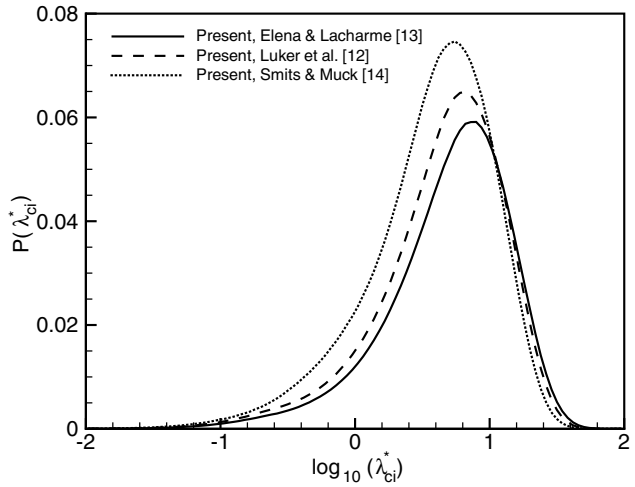

b)

Fig. 13 The effect of Reynolds number on a) mean values and b) probability density functions of the normalized swirling strengths.

downstream direction is found at $y_{\text{ref}}/\delta_0 = 0.3$. Also the correlation value at $y/\delta_0 = 0.9$ is nonnegligible (approximately 0.13). This implies that the wall-normal extent of the forward-leaning structure is comparable to the boundary-layer thickness. As the reference position is located farther away from the wall, the correlations appear more symmetric in the streamwise direction. These results are also consistent with previous findings in supersonic boundary layers [28,33]. Two-point correlations for the other cases show similar trends.

E. Integral Length Scale

Figure 15 shows the autocorrelation profiles of the streamwise velocity fluctuations for the Smits and Muck [14] case at $y_{\text{ref}}/\delta_0 = 0.2$ and 0.6 compared with those of Ganapathisubramani [33]. The computational and experimental results indicate that the correlations are consistently higher at $y_{\text{ref}}/\delta_0 = 0.2$ than at 0.6, which implies that larger streamwise structures are present. The present predictions show good agreement with experiment within $|\Delta x/\delta_0| \leq 0.25$, while significant differences are observed for larger separation distances. The results show that the correlations at $y_{\text{ref}}/\delta_0 = 0.2$ do not converge to zero level within the interrogation window but those at $y_{\text{ref}}/\delta_0 = 0.6$ converge, whereas the correlations for both locations did not converge in the experiment. This indicates that the streamwise integral length scale based on the autocorrelations within a short window can underpredict the true length scale. Therefore, we consider the integral length scale above $y_{\text{ref}}/\delta_0 \geq 0.3$, where the elongated tail of the autocorrelations is sufficiently captured within the window.

Figure 16 shows the variation of the streamwise integral length scale versus distance away from the wall. The results show that the integral length scale decreases from $0.7\delta_0$ to $0.4\delta_0$ as the outer edge of the boundary layer is approached. No significant differences in the normalized length scales are found for the three Reynolds numbers considered. The present length scales indicate an overprediction compared to the early experiments [34–40] listed in Dussauge and Smits [41], which show that the length scale varies between $0.1\delta_0$ and $0.6\delta_0$ for compressible boundary layers. They underpredict recent results [33] which used direct measurements of the spatial correlations and indicate that the length scales are at least 2 times larger than found in the early experiments. The proper quantitative estimation of integral length scales remains an open issue. However, the present results indicate that the integral length scale decreases in the outer part of the boundary layer, consistent with more recent observations [33], and that the length scales expressed using outer scaling have no significant dependence on Reynolds number.

F. Structure Angle

We calculate the average structure angle as a function of wall-normal distance using two-point spatial correlations of the streamwise fluctuating mass flux $(\rho u)'$. The corresponding correlations are defined as

$$R_a(\Delta x; y) = \frac{\overline{(\rho u)'(x, y, z) \cdot (\rho u)'(x + \Delta x, y + y_p, z)}}{\sigma_{(\rho u)'}(y)\sigma_{(\rho u)'}(y_p)} \tag{18}$$

where y_p is a probe separation distance. The correlations were spatiotemporally averaged in the streamwise and spanwise directions for 40 time realizations of the instantaneous flowfield. Note that the sampling distance of data sets in the spanwise direction is considered as the boundary-layer thickness to avoid interference of the turbulent structures. The domain of the correlation is limited as $-1 \leq \Delta x/\delta_0 \leq 1$ in the streamwise direction. Using ensemble-averaged correlations, the structure angle at different wall-normal locations is then computed as

$$\theta(y) = \tan^{-1}(y_p/x_p(y)) \tag{19}$$

where $x_p(y)$ is the peak location of the correlation at a given wall-normal distance y. The evaluation of the structure angle for each time realization can introduce a relative bias error in finding the peak position of the correlations, because the resolution of the structure angle is $\Delta\theta \approx 10$ deg near $\theta = 50$ deg for $y_p = 0.2\delta_0$. Ringuette et al. [42] evaluate the structure angle at each time and then average the data.

Figure 17 compares the average structure angles in the present simulation of the Smits and Muck [14] case with the results of Spina et al. [43] for four different probe separation distances ($y_p/\delta_0 = 0.09$, 0.21, 0.30, and 0.40). Note that the angles at the wall-normal distances ($y \geq \delta_0 - y_p$) where the correlation is very weak are excluded in the figure. It should be noticed that a smaller separation distance is able to detect better coherences in the turbulent structure but the resolution of the structure angle will be worse. The optimal distance used to define the structure angle will be dependent on the grid resolution of the simulation. In the present study, the separation distance $y_p/\delta_0 = 0.21$ gives the best results compared to the experimental results, while $y_p/\delta_0 = 0.05$ is found to be an optimum in the direct numerical simulation of Ringuette et al. [42]. The present results indicate that the structure angles in the outer part of the boundary layer vary from 54 deg $\leq \theta \leq$ 61 deg, whereas previous experiments [43,44] have reported a range of 45 to 60 deg for most of the boundary layer. We have extended the analysis of the structure angle to the Elena and Lacharme [13] and Luker et al. [12] cases based on the separation distance $y_p/\delta_0 = 0.2$. The results for the structure angle (Fig. 18) indicate no significant Reynolds-number dependence in the outer part of the boundary layer.

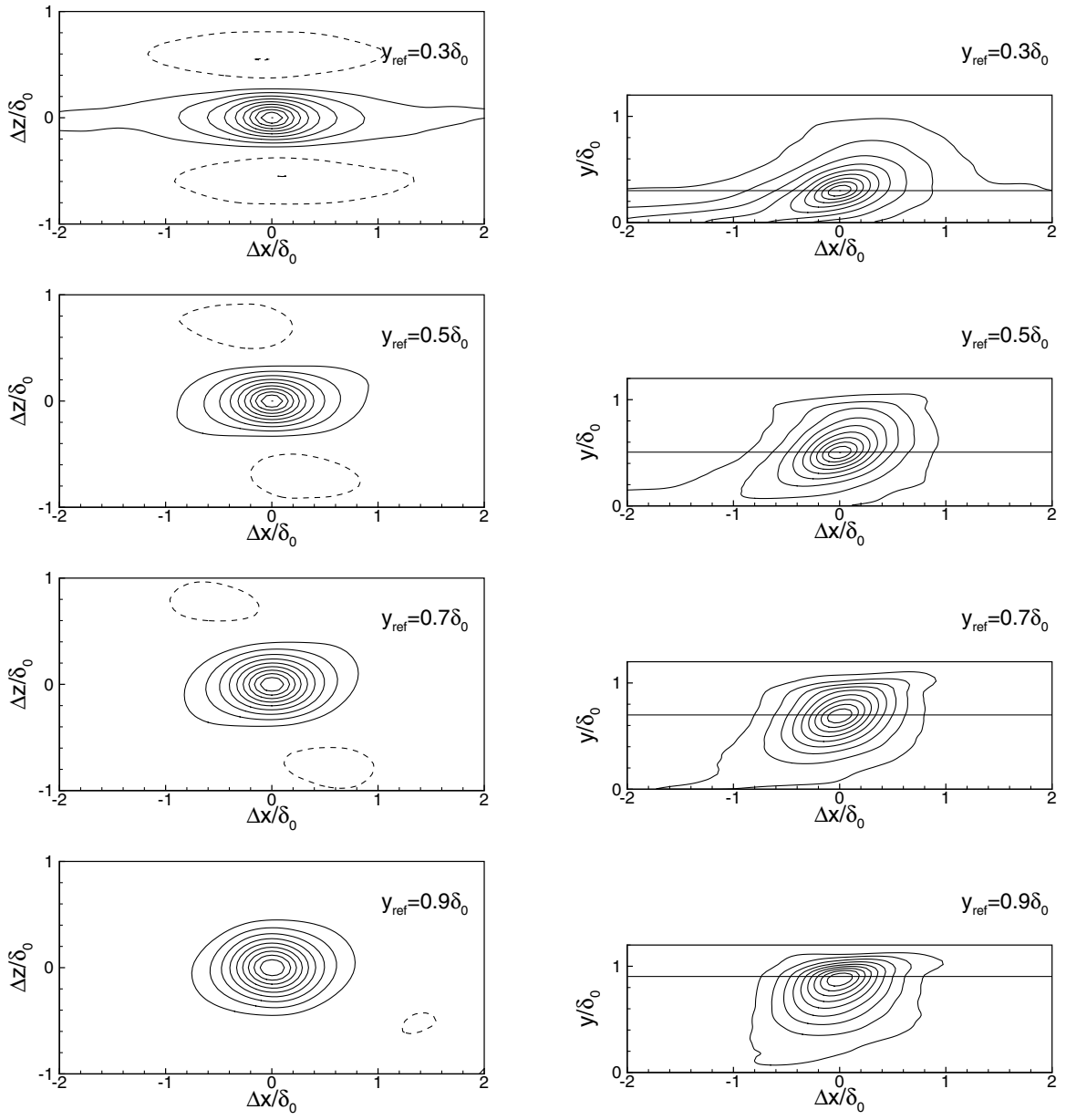

Fig. 14 Two-point correlations in a) the (x, z) plane and b) the (x, y) plane of streamwise velocity fluctuations at different wall-normal reference locations for the Smits and Muck [14] case.

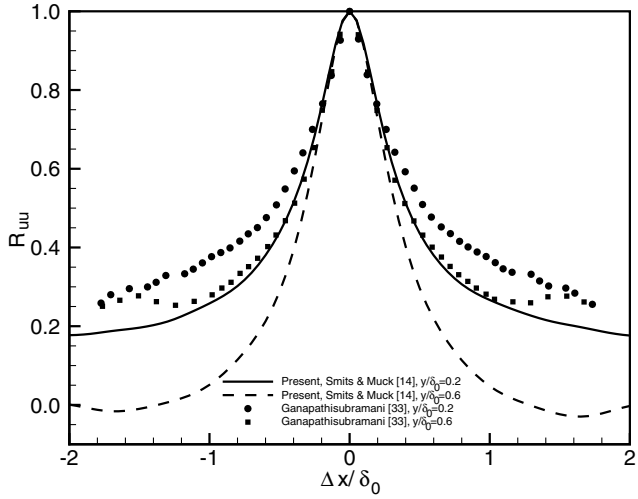

Fig. 15 Autocorrelations of streamwise velocity fluctuations at two wall-normal locations ($y/\delta_0 = 0.2$ and 0.6) for the Smits and Muck [14] case.

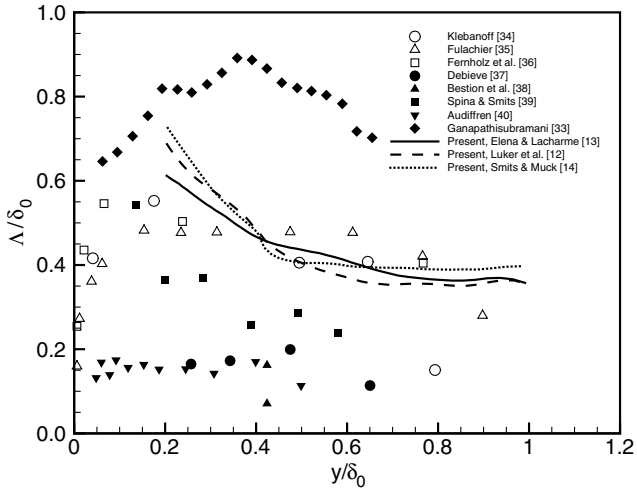

Fig. 16 Streamwise integral length scale in turbulent boundary layers.

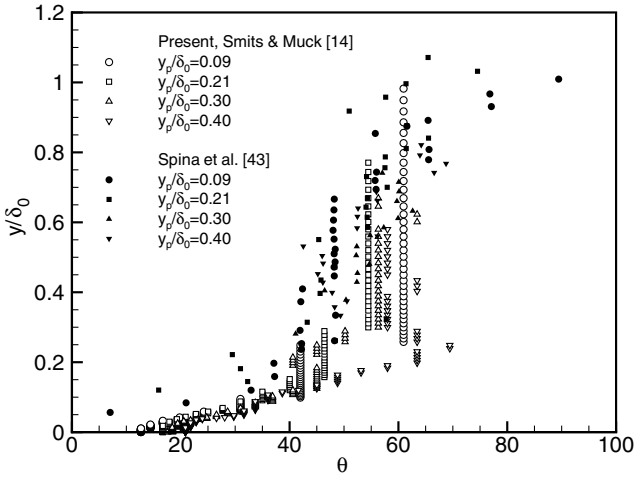

Fig. 17 Average structure angle based on different wall-normal probe separations for the Smits and Muck [14] case.

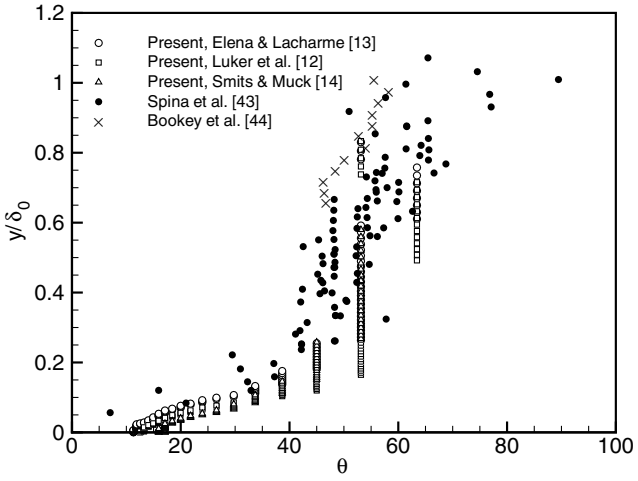

Fig. 18 The effect of Reynolds number on average structure angle.

V. Conclusions

Simulations of compressible boundary-layer flows at three different Reynolds numbers ($Re_\delta = 5.59 \times 10^4$, 1.78×10^5, and 1.58×10^6) have been performed using a hybrid large-eddy/Reynolds-averaged Navier–Stokes method. The model uses a flow-dependent RANS-to-LES transition function to shift the closure from Menter's two equation RANS model [7] near walls to the mixed subgrid-scale model [17] in the outer part of the boundary layer. To assess the present hybrid LES/RANS model, the effects of various modeling and algorithmic parameters on the predictions of mean-flow quantities and second-moment statistics have been determined. Structural features such as swirl strength, two-point correlations, integral length scales, and structure angles have also been determined, and the following conclusions can be stated:

1) The RANS/LES blending function should be designed to transition to LES toward the outer part of the logarithmic region for accurate predictions of the composite structure of the boundary layer and the Reynolds-shear stress levels.

2) Reconstructing the interface flux from extrapolated pressure and temperature (as opposed to extrapolated density and temperature) is more effective in suppressing grid-scale noise in the transverse-velocity components, and this leads to better predictions of the outer layer turbulent structure.

3) The choice of the variable-extrapolation method (fourth-order central versus fifth-order upwind biased) does not significantly influence predictions of the low-order turbulent statistics.

4) The choice of the recycling/rescaling strategy for the inflow properties does not significantly affect the predictions. All result in an adjustment distance of approximately $\sim 3\delta_0$ before the boundary layer begins to grow.

5) The use of a Klebanoff-type intermittency function to attenuate fluctuations in the outer part of the boundary layer helps keep the boundary-layer growth within the target range.

6) A resolution metric of 20 cells/boundary-layer thickness in the wall-transverse directions yields predictions almost identical to those obtained using 30 cells/boundary-layer thickness. Results obtained using only 10 cells/boundary-layer thickness in the wall-transverse directions are not grossly inferior to the refined-mesh results (at least for the Reynolds number tested), indicating that acceptable predictions of the boundary-layer structure might be obtained on meshes scaled according to the Escudier mixing length [19].

7) In general, the present hybrid LES/RANS model provides good predictions of mean-flow properties, second-moment boundary-layer statistics, and turbulence structural features. Reynolds-number independence in the outer layer is found to hold for second-moment statistics and structural features.

Appendix: Baseline Inflow Generation Method

The baseline inflow generation method is based on a recycling–rescaling procedure described by Edwards et al. [3], which is closely related to the technique presented by Urbin and Knight [8]. Fluctuations in the fluid properties at a *recycle* plane ($q = [\rho, u, v, w, T]$) are extracted by subtracting the instantaneous profile from a time- and span-averaged profile. The fluctuation fields are then rescaled according to boundary-layer similarity laws. Specific data locations at the inflow plane are filled by searching away from the wall for the positions where 1) the wall coordinates (d_w^+) at the recycle/inflow planes are matched, and 2) the d/δ values at the recycle and inflow planes are matched. Velocity fluctuations at the inflow plane are scaled by the ratio of the friction velocities at the recycle and inflow planes. This process yields two sets of fluctuating fields, which are then combined into one using a blending function defined in [6]. The rescaled fluctuations are superimposed onto a RANS mean inflow profile. Turbulence-model variables ($q = [k, \omega, \Gamma]$) are recycled and rescaled directly (without decomposing them into mean and fluctuating components). A Klebanoff-type intermittency function [Eq. (14)] multiplies the recycled and rescaled fluctuations to prevent excessive turbulence energy accumulation in the outer part of the boundary layer:

$$q_{\text{in}} = q_{\text{RANS}} + \Gamma_{\text{kleb}} q'_{\text{rec}} \quad \text{for primitive variables } q = [\rho, u, v, w, T] \tag{A1}$$

$$q_{\text{in}} = (1 - \Gamma_{\text{kleb}}) q_{\text{RANS}} + \Gamma_{\text{kleb}} q_{\text{rec}} \quad \text{for turbulence-model variables } q = [k, \omega, \Gamma] \tag{A2}$$

This procedure also ensures that the RANS freestream inflow properties are not altered outside the boundary layer. We also require that the recycled temperature fluctuations be no greater than allowed by Morkovin's hypothesis. From Morkovin's hypothesis,

$$C_p T'_{\text{mork}} = -[\Gamma_{\text{kleb}}(u_{\text{RANS}} u'_{\text{rec}} + v_{\text{RANS}} v'_{\text{rec}} + w_{\text{RANS}} w'_{\text{rec}}) + \tfrac{1}{2}\Gamma^2_{\text{kleb}}(u'^2_{\text{rec}} + v'^2_{\text{rec}} + w'^2_{\text{rec}})] \tag{A3}$$

and the recycled temperature fluctuation is limited as follows:

$$\Gamma_{\text{kleb}} T'_{\text{rec}}|_{\text{lim}} = \Gamma_{\text{kleb}} T'_{\text{rec}} \min(1.0, |T'_{\text{mork}}|/|\Gamma_{\text{kleb}} T'_{\text{rec}}|) \tag{A4}$$

To obtain a corrected value for the density fluctuation, we first introduce a provisional value of the pressure fluctuation as determined from the recycled density fluctuation:

$$p'_{\text{prov}} = R[\rho_{\text{RANS}} \Gamma_{\text{kleb}} T'_{\text{rec}}|_{\text{lim}} + \Gamma_{\text{kleb}} \rho'_{\text{rec}} (T_{\text{RANS}} + \Gamma_{\text{kleb}} T'_{\text{rec}}|_{\text{lim}})] \tag{A5}$$

We then require that the pressure fluctuation be limited to a user-specified multiple of the mean pressure (2% in the cases described herein):

$$p'_{\text{prov}}|_{\text{lim}} = p'_{\text{prov}} \min(1.0, 0.02 p_{\text{RANS}}/|p'_{\text{prov}}|) \tag{A6}$$

Finally, we obtain the corrected value of the density fluctuation from the limited pressure and temperature fluctuations:

$$\rho'_{\text{rec}} = (p'_{\text{prov}}|_{\text{lim}} - \rho_{\text{RANS}} R \Gamma_{\text{kleb}} T'_{\text{rec}}|_{\text{lim}})/R(T_{\text{RANS}} + \Gamma_{\text{kleb}} T'_{\text{rec}}|_{\text{lim}}) \tag{A7}$$

Acknowledgments

This work is supported by NASA under Cooperative Agreement NNX07AC27A-S01. Computer resources have been provided by the High Performance Computing component of North Carolina State University's Information Technology division.

References

[1] Wu, M., and Martín, M. P., "Analysis of Shock Motion in Shockwave and Turbulent Boundary Layer Interaction Using Direct Numerical Simulation Data," *Journal of Fluid Mechanics*, Vol. 594, Jan. 2008, pp. 71–83. doi:10.1017/S0022112007009044

[2] Loginov, M. S., Adams, N. A., and Zheltovodov, A., "Large-Eddy Simulation of Shock-Wave/Turbulent-Boundary-Layer Interaction," *Journal of Fluid Mechanics*, Vol. 565, Oct. 2006, pp. 135–169. doi:10.1017/S0022112006000930

[3] Edwards, J. R., Choi, J.-I., and Boles, J. A., "Hybrid LES/RANS Simulation of a Mach 5 Compression-Corner Interaction," *AIAA Journal*, Vol. 46, No. 4, 2008, pp. 977–991. doi:10.2514/1.32240

[4] Baurle, R. A., Tam, J., Edwards, J. R., and Hassan, H. A., "Hybrid Simulation Approach for Cavity Flows: Blending, Algorithm, and Boundary Treatment Issues," *AIAA Journal*, Vol. 41, No. 8, 2003, pp. 1463–1480. doi:10.2514/2.2129

[5] Fan, T. C., Edwards, J. R., Hassan, H. A., and Baurle, R. A., "Hybrid Large-Eddy/Reynolds-Averaged Navier-Stokes Simulations of Shock-Separated Flows," *Journal of Spacecraft and Rockets*, Vol. 41, No. 6, 2004, pp. 897–906. doi:10.2514/1.3735

[6] Xiao, X., Edwards, J. R., Hassan, H. A., and Baurle, R. A., "Inflow Boundary Conditions for Hybrid Large-Eddy/Reynolds-Averaged Navier-Stokes Simulations," *AIAA Journal*, Vol. 41, No. 8, 2003, pp. 1481–1490. doi:10.2514/2.2130

[7] Menter, F. R., "Two-Equation Eddy-Viscosity Turbulence Models for Engineering Applications," *AIAA Journal*, Vol. 32, No. 8, 1994, pp. 1598–1605. doi:10.2514/3.12149

[8] Urbin, G., and Knight, D., "Large Eddy Simulation of a Supersonic Boundary Layer Using an Unstructured Grid," *AIAA Journal*, Vol. 39, No. 7, 2001, pp. 1288–1295. doi:10.2514/2.1471

[9] Stolz, S., and Adams, N. A., "Large-Eddy Simulation of High-Reynolds-Number Supersonic Boundary Layers Using the Approximate Deconvolution Model and a Rescaling and Recycling Technique," *Physics of Fluids*, Vol. 15, No. 8, 2003, pp. 2398–2412. doi:10.1063/1.1588637

[10] Xu, S., and Martín, M. P., "Assessment of Inflow Boundary Conditions for Compressible Turbulent Boundary Layers," *Physics of Fluids*, Vol. 16, No. 7, 2004, pp. 2623–2639. doi:10.1063/1.1758218

[11] Sagaut, P., Garnier, E., Tromeur, E., Larchevêque, L., and Labourasse, E., "Turbulent Inflow Conditions for Large-Eddy Simulation of Compressible Wall-Bounded Flows," *AIAA Journal*, Vol. 42, No. 3, 2004, pp. 469–477. doi:10.2514/1.3461

[12] Luker, J. J., Bowersox, R. D. W., and Buter, T. A., "Influence of Curvature-Driven Favorable Pressure Gradient on Supersonic Turbulent Boundary Layer," *AIAA Journal*, Vol. 38, No. 8, 2000, pp. 1351–1359. doi:10.2514/2.1134

[13] Elena, M., and Lacharme, J. P., "Experimental Study of a Supersonic Turbulent Boundary Layer Using a Laser Doppler Anemometer," *Journal de Mecanique Theorique et Appliquee*, Vol. 7, No. 2, 1988, pp. 175–190.

[14] Smits, A. J., and Muck, K.-C., "Experimental Study of Three Shock-Wave/Turbulent Boundary Layer Interactions," *Journal of Fluid Mechanics*, Vol. 182, Sept. 1987, pp. 291–314. doi:10.1017/S0022112087002349

[15] Roy, C. J., and Edwards, J. R., "Numerical Simulation of a Three-Dimensional Flame/Shock Wave Interaction," *AIAA Journal*, Vol. 38, No. 5, 2000, pp. 745–754. doi:10.2514/2.1035

[16] Edwards, J. R., "A Low-Diffusion Flux-Splitting Scheme for Navier-Stokes Calculations," *Computers and Fluids*, Vol. 26, No. 6, 1997, pp. 635–639. doi:10.1016/S0045-7930(97)00014-5

[17] Lenormand, E., Sagaut, P., Ta Phuoc, L., and Comte, P., "Subgrid-Scale Models for Large-Eddy Simulations of Compressible, Wall-Bounded Flows," *AIAA Journal*, Vol. 38, No. 8, 2000, pp. 1340–1350. doi:10.2514/2.1133

[18] Colella, P., and Woodward, P. R., "The Piecewise Parabolic Method (PPM) for Gas-Dynamical Simulations," *Journal of Computational Physics*, Vol. 54, April 1984, pp. 174–201. doi:10.1016/0021-9991(84)90143-8

[19] Wilcox, D. C., *Turbulence Modeling for CFD*, 2nd ed., DCW Industries, La Caňada, CA, 1998.

[20] Miller, R., Dotter, J., Bowersox, R. D. W., and Buter, T. A., "Compressible Turbulence Measurements in Supersonic Boundary Layers with Favorable and Adverse Pressure Gradients," *Transitional and Turbulent Compressible Flows*, edited by E. F. Spina and C. Arakawa, FED-Vol. 224 (American Society of Mechanical Engineers, New York, 1995), pp. 193–200.

[21] Fernando, E. M., and Smits, A. J., "A Supersonic Turbulent Boundary Layer in an Adverse Pressure Gradient," *Journal of Fluid Mechanics*, Vol. 211, Feb. 1990, pp. 285–307. doi:10.1017/S0022112090001574

[22] Johnson, D. A., and Rose, W. C., "Laser Velocimeter and Hot-Wire Anemometer Comparison in a Supersonic Boundary Layer," *AIAA Journal*, Vol. 13, No. 4, 1975, pp. 512–515. doi:10.2514/3.49739

[23] Robinson, S. K, Seegmiller, M. L., and Kussoy, M. I., "Hot-Wire and Laser Doppler Anemometer Measurements in a Supersonic Boundary Layer," AIAA Paper 83-1723, 1983.

[24] Martín, M. P., "Direct Numerical Simulation of Hypersonic Turbulent Boundary Layers. Part 1: Initialization and Comparison with Experiment," *Journal of Fluid Mechanics*, Vol. 570, Jan. 2007, pp. 347–364. doi:10.1017/S0022112006003107

[25] Smits, A. J., and Dussauge, J.-P., *Turbulent Shear Layers in Supersonic Flow*, 2nd ed., Springer Science & Business Media Inc., New York, 2006.

[26] Fernholz, H. H., and Finley, P. J., "The Incompressible Zero-Pressure-Gradient Turbulent Boundary Layer: An Assessment of the Data," *Progress in Aerospace Sciences*, Vol. 32, No. 4, 1996, pp. 245–311. doi:10.1016/0376-0421(95)00007-0

[27] Selig, M. S., Andreopoulos, J., Muck, K.-C., Dussauge, J. P., and Smits, A. J., "Turbulent Structure in a Shock Wave/Turbulent Boundary-Layer Interaction," *AIAA Journal*, Vol. 27, No. 7, 1989, pp. 862–869. doi:10.2514/3.10193

[28] Smits, A. J., Spina, E. F., Alving, A. E., Smith, R. W., Fernando, E. M., and Donovan, J. F., "A Comparison of the Turbulence Structure of Subsonic and Supersonic Boundary Layers," *Physics of Fluids A*, Vol. 1, No. 11, 1989, pp. 1865–1875. doi:10.1063/1.857511

[29] Donovan, J. F., Spina, E. F., and Smits, A. J., "The Structure of a Supersonic Turbulent Boundary Layer Subjected to Concave Surface Curvature," *Journal of Fluid Mechanics*, Vol. 259, Jan. 1994, pp. 1–24. doi:10.1017/S0022112094000017

[30] Maeder, T., Adams, N. A., and Kleiser, L., "Direct Numerical Simulation of Turbulent Supersonic Boundary Layers by an Extended Temporal Approach," *Journal of Fluid Mechanics*, Vol. 429, Feb. 2001, pp. 187–216. doi:10.1017/S0022112000002718

[31] Zhou, J., Adrian, R. J., Balachandar, S., and Kendall, T. M., "Mechanisms for Generating Coherent Packets of Hairpin Vortices in Channel Flow," *Journal of Fluid Mechanics*, Vol. 387, May 1999, pp. 353–396. doi:10.1017/S002211209900467X

[32] Ganapathisubramani, B., Clemens, N. T., and Dolling, D. S., "Large-Scale Motions in a Supersonic Turbulent Boundary Layer," *Journal of Fluid Mechanics*, Vol. 556, June 2006, pp. 271–282. doi:10.1017/S0022112006009244

[33] Ganapathisubramani, B., "Statistical Properties of Streamwise Velocity in a Supersonic Turbulent Boundary Layer," *Physics of Fluids*, Vol. 19, No. 9, 2007, p. 098108. doi:10.1063/1.2772303

[34] Klebanoff, P. S., "Characteristics of Turbulence in a Boundary Layer with Zero Pressure Gradient," NACA Rept. 1247, 1955.

[35] Fulachier, L., "Contribution à l'étude des Analogies des Champs Dynamiques et Thermiques dans une Chouche Limite Turbulente. Effet de l'Aspiration," Ph.D. Thesis, Université de Provence, Aix-Marseille, 1972.

[36] Fernholz, H. H., Krause, E., Nockemann, N., and Schober, M., "Comparative Measurements in the Canonical Boundary Layer at $Re_{\delta 2} > 6 \times 10^4$ on the Wall of the German-Dutch Wind Tunnel," *Physics of Fluids*, Vol. 7, No. 6, 1995, pp. 1275–1281. doi:10.1063/1.868516

[37] Debiève, J. F., "Étude d'une Interaction Turbulence/onde de choc," Ph.D. Thesis, Université d'Aix-Marseille II, 1983.

[38] Bestion, D., Debiève, J. F., and Dussauge, J. P., "Two Rapid Distortions in Supersonic Flows: Turbulence/Shock Wave and Turbluence/Expansion," *Structure of Complex Turbulent Shear Flows*, edited by R. Dumas, and L. Fulachier, Springer–Verlag, Berlin, 1983.

[39] Spina, E. F., and Smits, A. J., "Organized Structures in a Compressible Boundary Layer," *Journal of Fluid Mechanics*, Vol. 182, 1987, pp. 85–109. doi:10.1017/S0022112087002258

[40] Audiffren, N., "Turbulence d'une Couche Limite Soumise à une Variation de Densité due à une onde de choc ou à un Chauffage Parietal, Ph.D. Thesis, Université d'Aix-Marseille II, 1993.

[41] Dussauge, J. P., and Smits, A. J., "Characteristic Scales for Energetic Eddies in Turbulent Supersonic Boundary Layers," *Experimental Thermal and Fluid Science*, Vol. 14, No. 1, 1997, pp. 85–91. doi:10.1016/S0894-1777(96)00104-5

[42] Ringuette, M. J., Martín, M. P., Smits, A. J., and Wu, M., "Characterization of the Turbulence Structure in Supersonic Boundary Layers Using DNS Data," AIAA Paper 2006-3539, June 2006.

[43] Spina, E. F., Donovan, J. F., and Smits, A. J., "On the Structure of High-Reynolds Number Supersonic Turbulent Boundary Layers," *Journal of Fluid Mechanics*, Vol. 222, Jan. 1991, pp. 293–327. doi:10.1017/S0022112091001118

[44] Bookey, P., Wyckham, C., Smits, A. J., and Martín, M. P., "New Experimental Data of STBLI at DNS/LES Accessible Reynolds Numbers," AIAA Paper 2005-0309, Jan. 2005.

P. Givi
Associate Editor